ADVANCED MATERIALS INTERFACES

Supporting Information

for *Adv. Mater. Interfaces,* DOI: 10.1002/admi.201701003

Unlocking the Single-Domain Epitaxy of Halide Perovskites

*Lili Wang, Pei Chen, Non Thongprong, Margaret Young, Padmanaban S. Kuttipillai, Chuanpeng Jiang, Pengpeng Zhang, Kai Sun, Phillip M. Duxbury, and Richard R. Lunt**

WILEY-VCH

Supporting Information

Unlocking the Single-Domain Epitaxy of Halide Perovskites

Dr. Lili Wang[a,†], Pei Chen[a,†], Dr. Non Thongprong[b], Margaret Young[a], Padmanaban S. Kuttipillai[a], Chuanpeng Jiang[b], Prof. Pengpeng Zhang[b], Dr. Kai Sun[c], Prof. Phillip M. Duxbury[b], Prof. Richard R. Lunt[a,b,]*

Correspondence to: rlunt@msu.edu

This PDF file includes:

Figs. S1 to S25
Tables S1 to S6
Captions for Movies S1
Supplementary Text

Other Supplementary Materials for this manuscript includes the following:

Movies S1

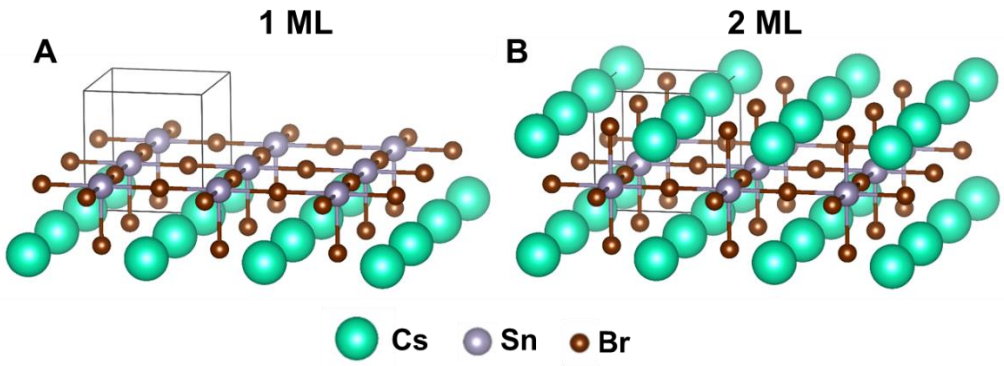

Figure S1. Schematic crystal structure of cubic $CsSnBr_3$. (A) monolayer and (B) bilayer (i.e., 1 unit cell). Green spheres are Cs; gray spheres are Sn; red spheres are Br. For cubic $CsSnBr_3$, the lattice constant is 5.8 Å; therefore, the monolayer (ML) and bilayer (BL) thicknesses are defined as *a/2* (2.9 Å) and *a* (5.8 Å), respectively.

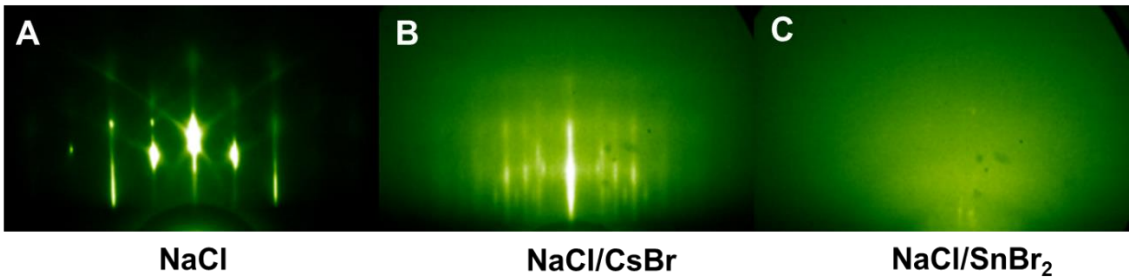

Figure S2. RHEED patterns of substrate and precursors. (A) NaCl along the [110], (B) CsBr and (C) $SnBr_2$ with 22 Å thickness.

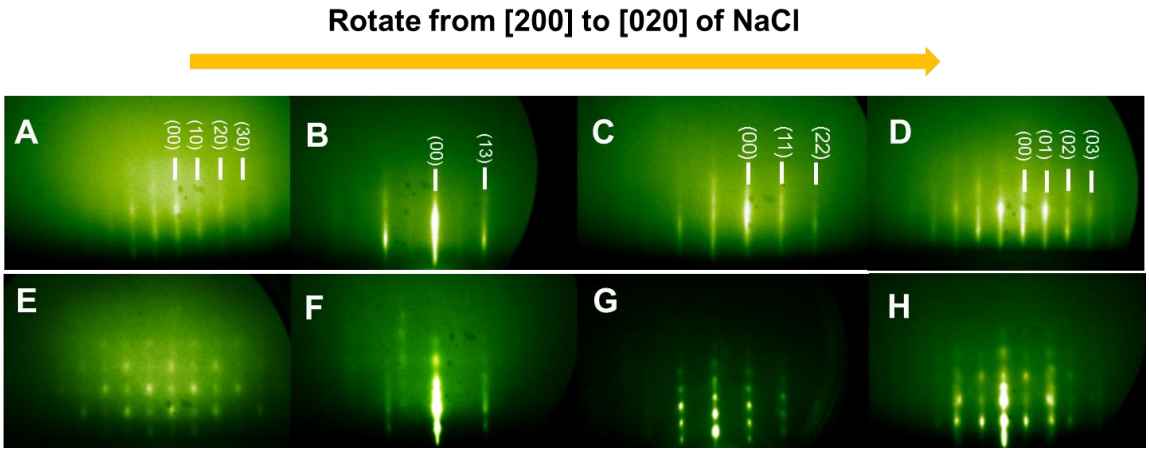

Figure S3. Rotation dependent RHEED patterns. Streaky RHEED patterns of (A-D) cubic phase $CsSnBr_3$ taken from different rotation angles showing that single-domain epitaxial layer is formed on the substrates. RHEED patterns of roughened (E-H) tetragonal phase $CsSn_2Br_5$ taken from different rotation angles.

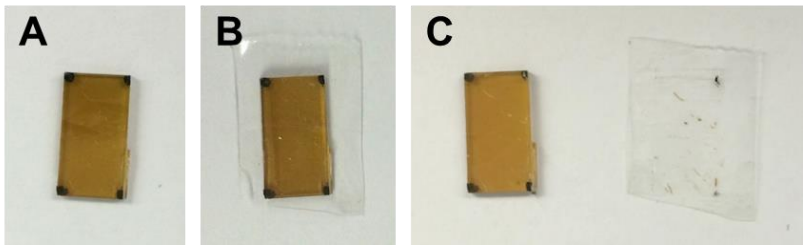

Figure S4. Film adhesion of the epitaxial growth of $CsSnBr_3$ on NaCl. (A) Epitaxial $CsSnBr_3$ sample before application of Scotch tape; (B) after attachment on the film surface; and (C) after peeling off.

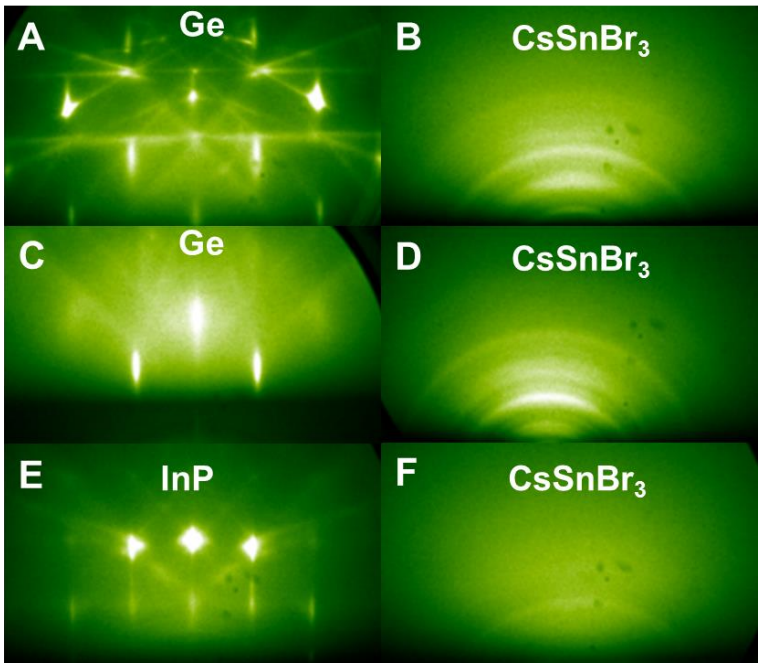

Figure S5. RHEED patterns of growth of $CsSnBr_3$ on Ge and InP. (A) Ge single crystalline substrate along the [100]; (B) $CsSnBr_3$ grown on Ge; (C) Ge single crystalline substrate along the [100] pre-treated with HCl acid etching for 30s; (D) $CsSnBr_3$ grown on Ge from (C); (E) InP single crystalline substrate along the [100]; (F) $CsSnBr_3$ grown on InP.

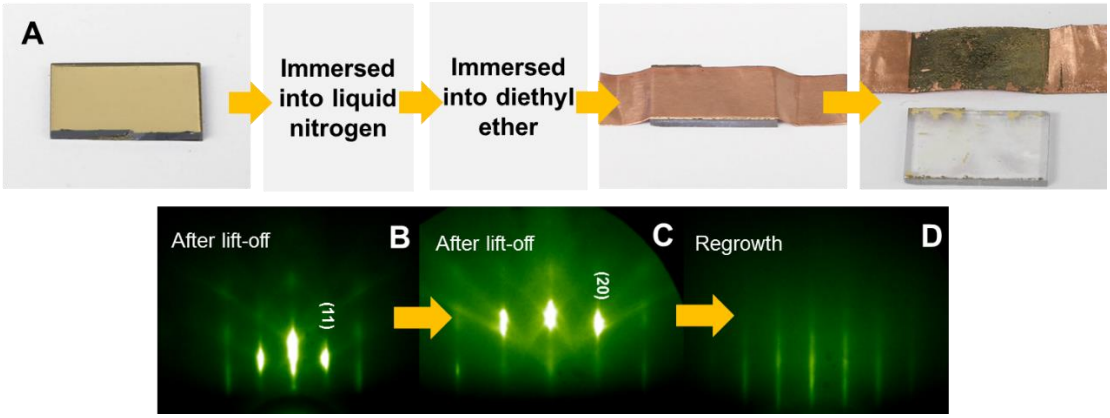

Figure S6. Epitaxy lift-off and regrowth. (A) Epitaxial lift-off procedure: the epitaxial $CsSnBr_3$ grown on NaCl with a gold layer (~300 Å) on the top is rapidly immersed into liquid nitrogen and then rapidly transferred into diethyl ether; Cu tape is then pressed onto the surface and then slowly peeled which results in separation of the epitaxial film from the substrate; (B-D) RHEED patterns for the epitaxial re-growth of $CsSnBr_3$ after epitaxial lift-off.

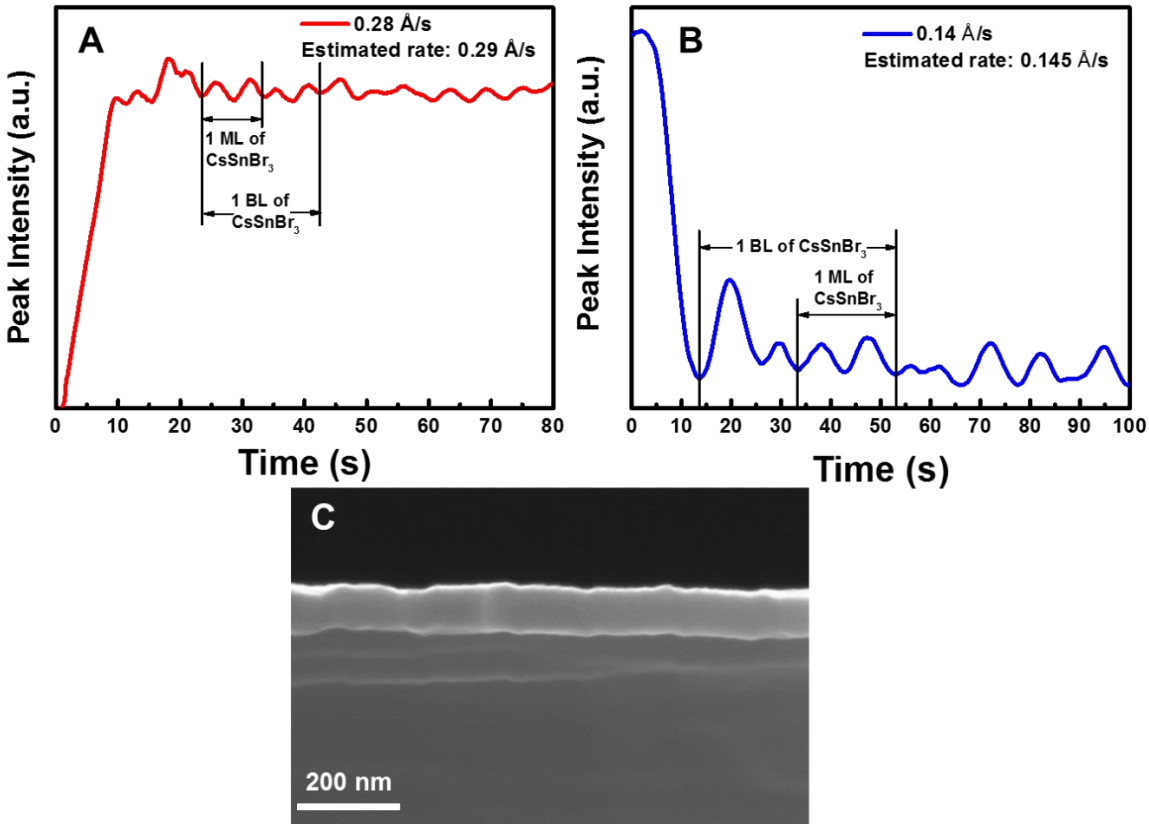

Figure S7. RHEED oscillations. Specular RHEED intensity recorded during $CsSnBr_3$ epitaxial growth at 1:1 stoichiometry on NaCl at (A) 0.28 Å/s and (B) 0.14 Å/s. The oscillation period is 5 s and 10 s for (A) and (B), respectively, and corresponds to

thickness of a half monolayer. (C) Cross-section SEM image used for calibration of the growth rate.

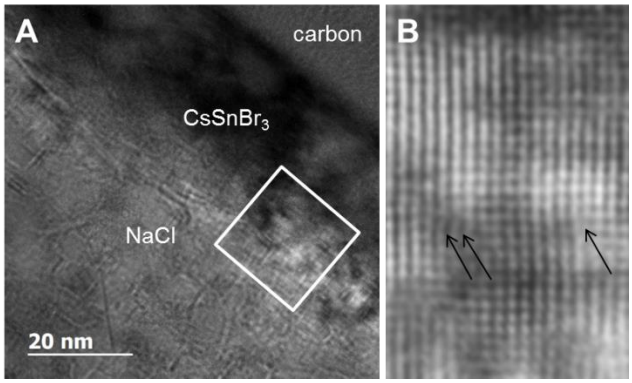

Figure S8. Investigation of interface between epitaxial $CsSnBr_3$ and NaCl. (A) Cross-section TEM images of NaCl/$CsSnBr_3$ (~25 nm). The area marked with a white frame in (A) is enlarged and shown in Figure 2a. (B) Same area shown in Figure 2b with black arrows marking dislocations.

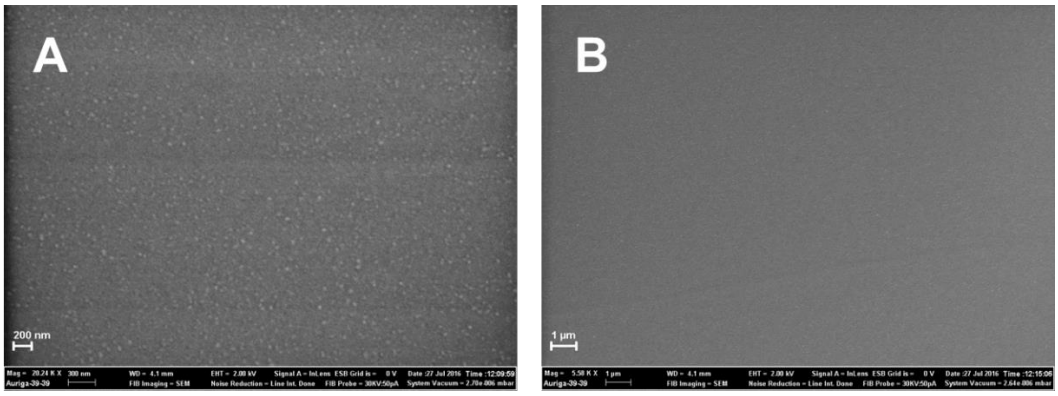

Figure S9. Top-view SEM images of epitaxial $CsSnBr_3$ on NaCl. The scale bar in **(**A) is 200 nm, in (B) is 1 µm. The small dots shown on the surface are Pt nanoparticles deposited to avoid charging on the surface.

Identification of $CsSn_2Br_5$

$CsSn_2Br_5$ has a bulk tetragonal structure with lattice constants of a = 8.48 Å and c = 15.28 Å.[1] The d-spacings along the substrate normal and along in-plane axes parallel to the NaCl [110] are 7.58±0.12 Å and 3.77±0.05 Å, respectively. The RHEED pattern of the tetragonal phase along NaCl [110] is consistent with the simulated SAED pattern of $CsSn_2Br_5$ along the [210] direction (shown below), i.e. $(001)[110]_{NaCl}//(002)[210]_{CsSn_2Br_5}$. Therefore, the measured lattice constants of the tetragonal $CsSn_2Br_5$ are a = 8.43±0.11 Å and c = 15.16±0.24 Å, which is within error of the value reported in Ref[1].

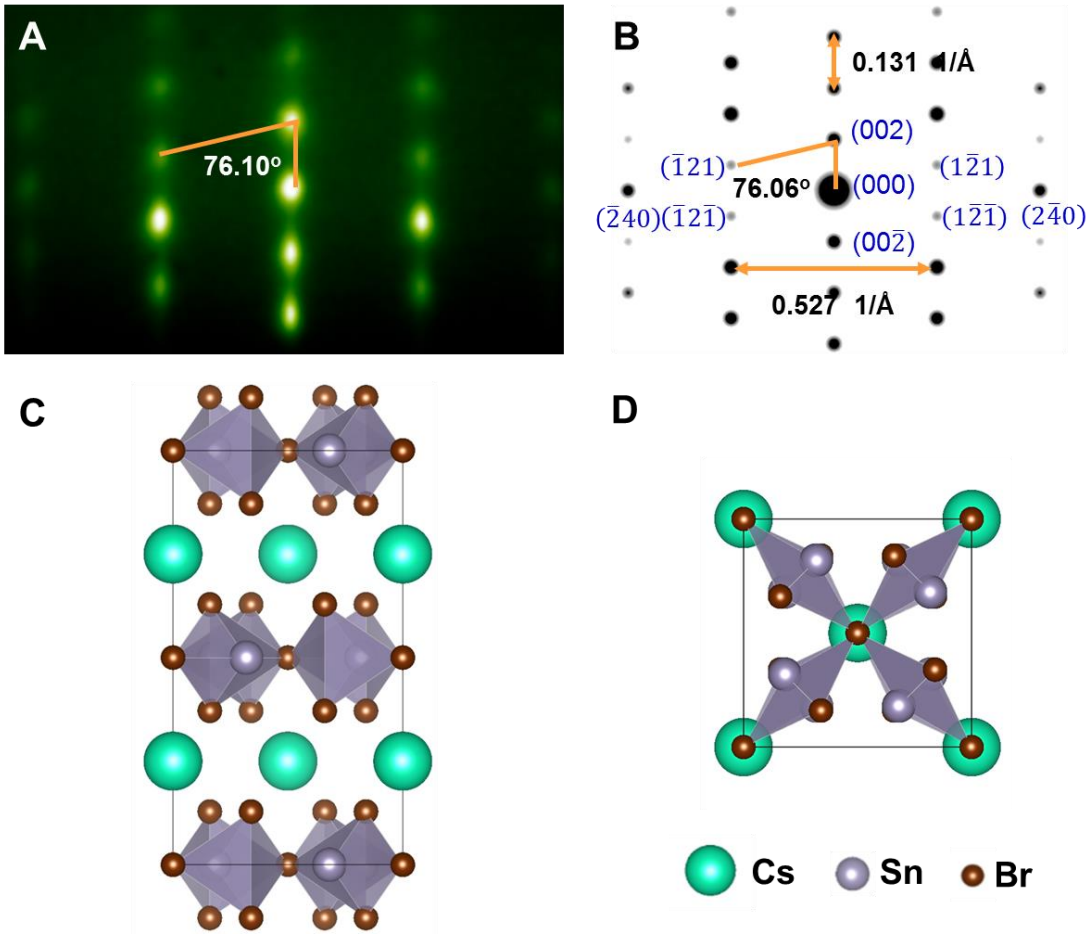

Figure S10. RHEED pattern, simulated SAED and crystal structure of tetragonal $CsSn_2Br_5$. (A) RHEED pattern of the sample grown at the ratio of 0.25:1 ($CsBr:SnBr_2$) collected along the [110] direction of NaCl. (B) Simulated SAED pattern of $CsSn_2Br_5$ along the [210] direction. The calculated d-spacings of (002) and (210) are 7.63 Å and 3.79 Å, respectively, which are consistent with the values calculated from the RHEED pattern (7.58±0.12 Å and 3.77±0.05 Å). Schematic illustration of the crystal structure of $CsSn_2Br_5$ viewed along (C) a-axis and (D) c-axis. Green spheres are Cs; gray spheres are Sn; red spheres are Br.

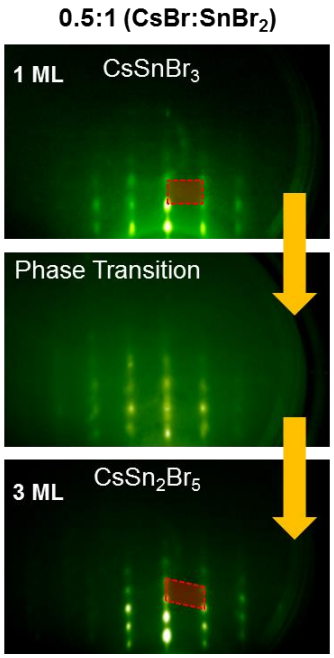

Figure S11. *In-situ* real-time monitoring of the phase transition. A phase transition from the cubic to tetragonal phase occurs when the deposition ratio of CsBr to $SnBr_2$ is 0.5:1 after 1-2 monolayers. Note that while the pattern for the tetragonal phase appears monoclinic, it is actually a rotated tetragonal phase as shown in Fig. S4 and the diffraction spots are therefore not along primary axes.

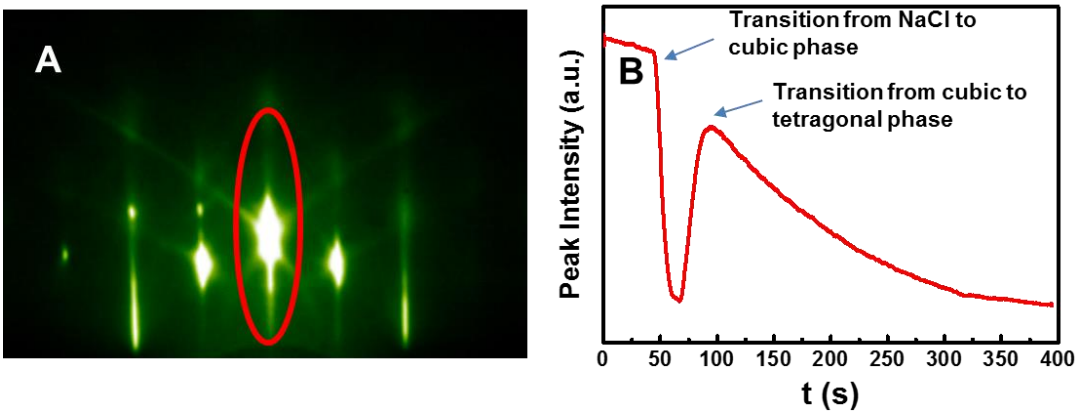

Figure S12. RHEED oscillations monitored during growth process. (A) RHEED pattern with the monitored intensity area highlighted with the red circle and the corresponding (B) RHEED intensity profile with time.

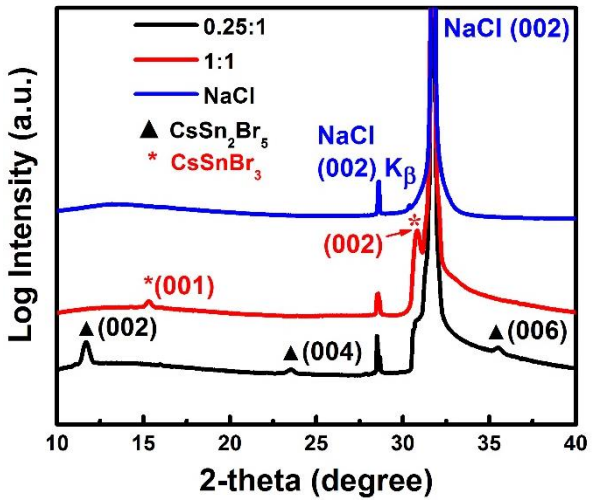

Figure S13. Crystal structure characterization of the two epitaxial phases. (A) XRD patterns of NaCl (blue curve) and samples grown at different ratios of CsBr:$SnBr_2$: 0.25:1 (black curve) and 1:1 (red curve).

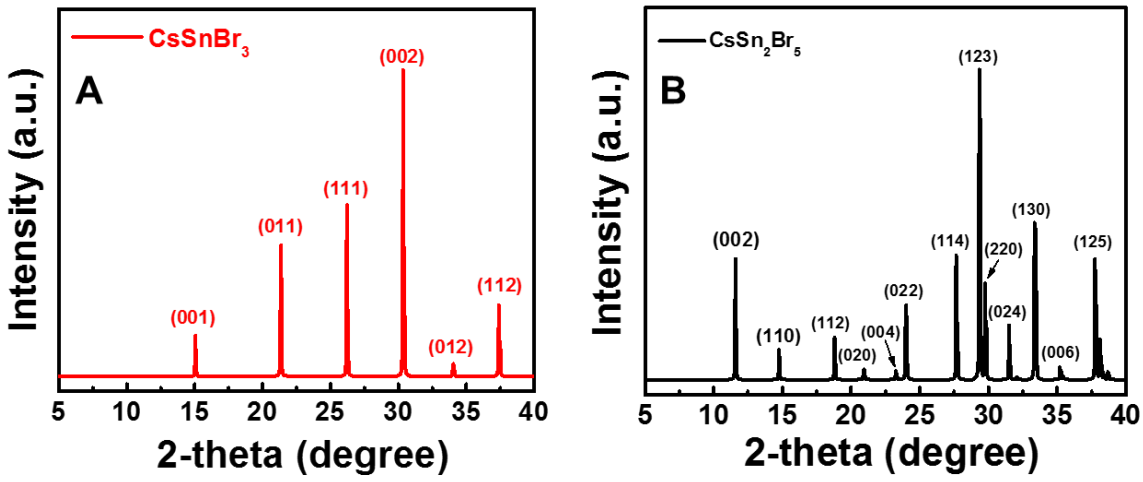

Figure S14. Calculated XRD patterns. (A) cubic $CsSnBr_3$ and (B) tetragonal $CsSn_2Br_5$.

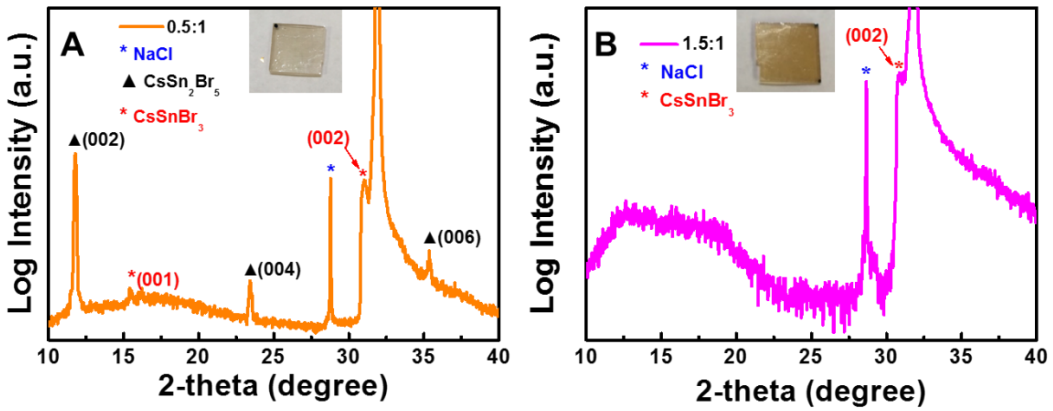

Figure S15. XRD patterns of samples grown at different precursor ratios. (A) 0.5:1 and (B) 1.5:1 of CsBr to $SnBr_2$. The insets show the appearance of samples prepared at 0.5:1 and 1.5:1 ratio, respectively. It shows both phases ($CsSnBr_3$ and $CsSn_2Br_5$) occur when the sample is prepared at 0.5:1 ratio.

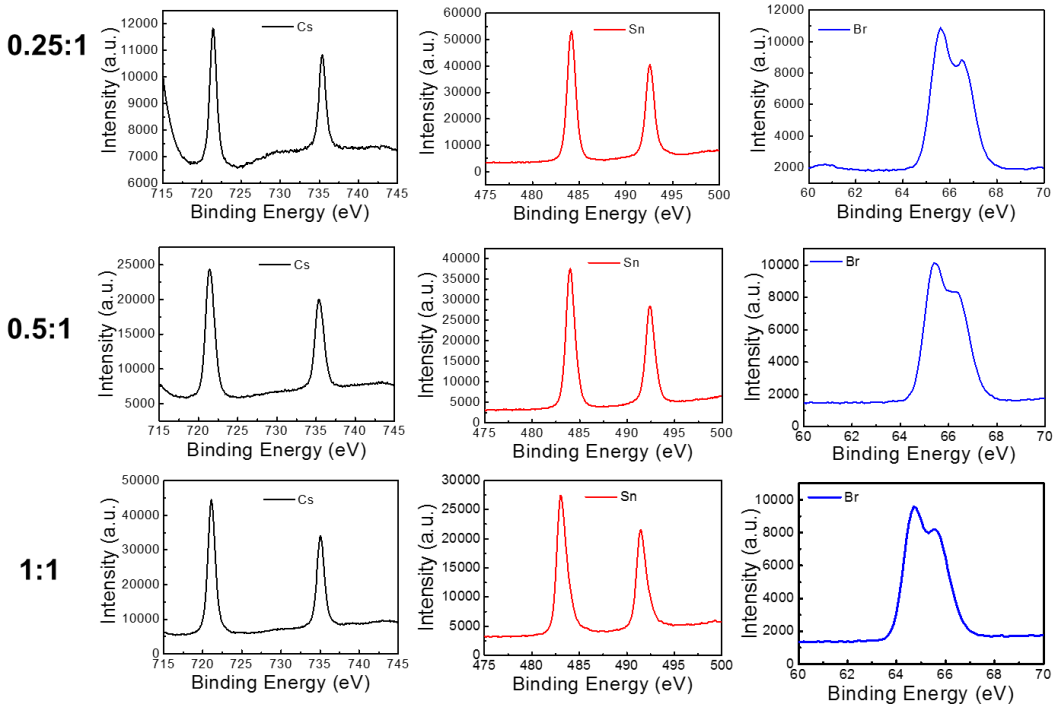

Figure S16. XPS spectra of samples grown at different precursor ratios. All the spectra were taken at the top surfaces of the epitaxial film. From the sensitivity factors and the peak area of binding energy of different elements (Cs, Sn, Br), the elemental ratio is obtained.

XPS of $CsSn_2Br_5$ sputtered by Ar^+ ion

When prepared with a 0.25:1 ratio, the atomic concentration of Cs is much lower than that of Sn and Br. However, after Ar^+ sputtering of the top surface, the atomic concentration of Cs increases, and the elemental ratio is close to stoichiometric $CsSn_2Br_5$ (1:2:5 for Cs:Sn:Br) (as shown in fig. S17 and Table S3). This suggests that the Cs vacancies concentrated at the interface are likely eliminated as the growth proceeds or subsequently concentrated as the growth is halted.

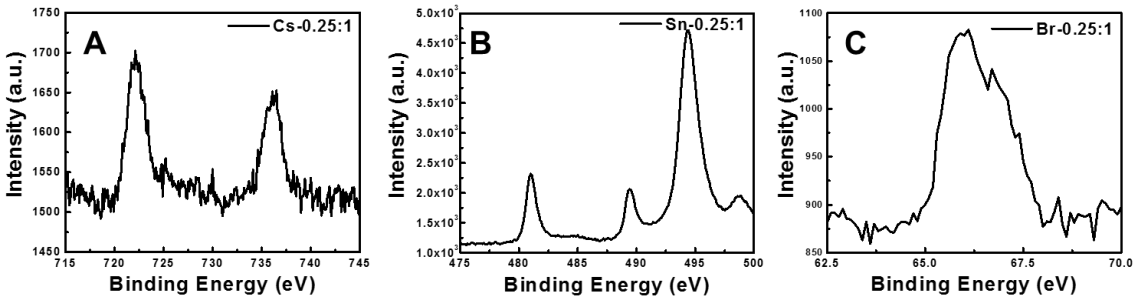

Figure S17. XPS spectra of $CsSn_2Br_5$ after Ar^+ ion sputtering. It should be noted that Sn^{2+} is partially reduced by Ar^+ during sputtering (1.5 mins), resulting in the Sn3d peak splitting; however, this does not change the molar ratios calculated by integrating the peak area of different elements divided with sensitivity factors.

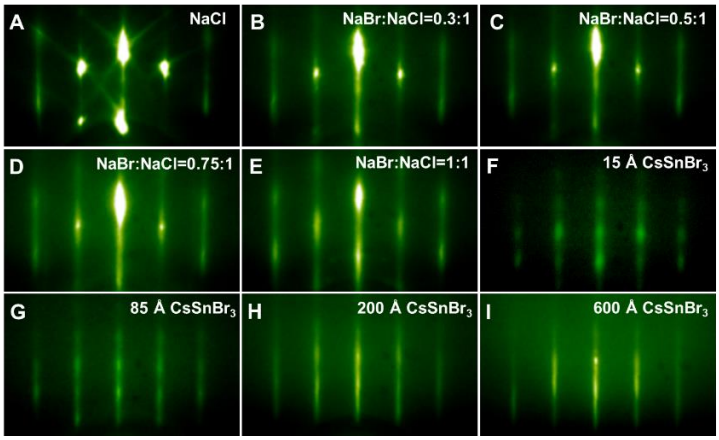

Figure S18. Epitaxial growth of $CsSnBr_3$ on pseudomorphic interlayers of NaCl-NaBr. (A-E) RHEED patterns of growth of pseudomorphic interlayers of NaCl-NaBr on NaCl substrates. The ratio of NaBr: NaCl is gradually increased to reduce the misfit between substrates and interlayers. Note that when the ratio of NaBr: NaCl reaches 1:1, the lattice constant of interlayers is 5.81 Å perfectly matching that of $CsSnBr_3$ (5.80 Å). During the growth, the lattice constant calculated from RHEED patterns shows gradual increase along with increasing the ratio of NaBr: NaCl. **(**F-I) RHEED patterns of growth of $CsSnBr_3$ on pseudomorphic interlayers of NaCl-NaBr.

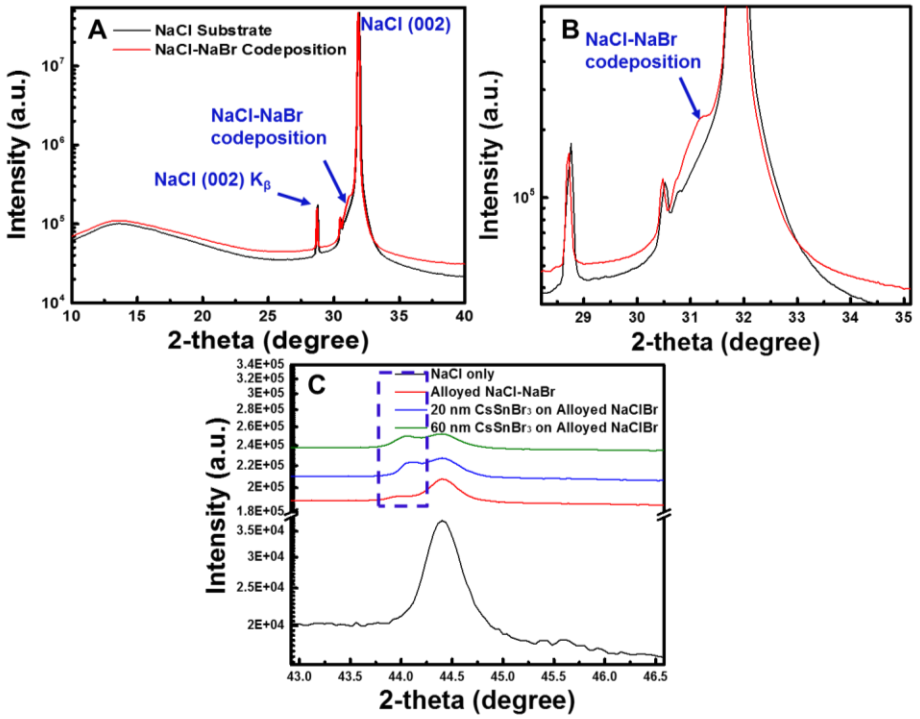

Figure S19. XRD patterns of alloyed NaCl-NaBr pseudomorphic interlayers and $CsSnBr_3$. (A) Comparison of NaCl substrate alone and alloyed NaCl-NaBr layers. (B) Enlarged view of (A) shows a shoulder peak arises in the sample of alloyed NaCl-NaBr pseudomorphic interlayers on NaCl substrates. **(**C) Enlarged view shows the peak splitting that reflects the change of lattice constant from NaCl substrate, alloyed NaCl-NaBr, and $CsSnBr_3$.

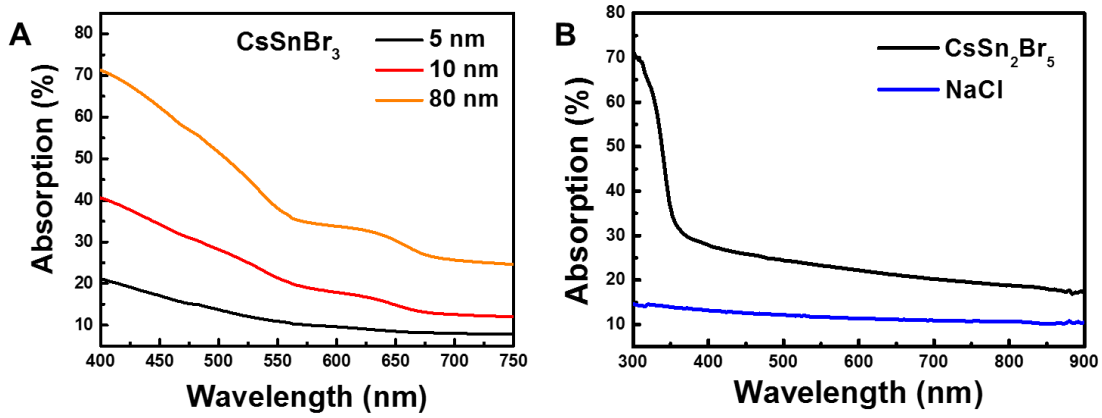

Figure S20. Absorption spectra of two phases and NaCl substrate. (A) $CsSnBr_3$ of varying well thickness and (B) $CsSn_2Br_5$ (black curve) and NaCl (blue curve). The spectra are converted from (1-Transmission) and shifted for clarity.

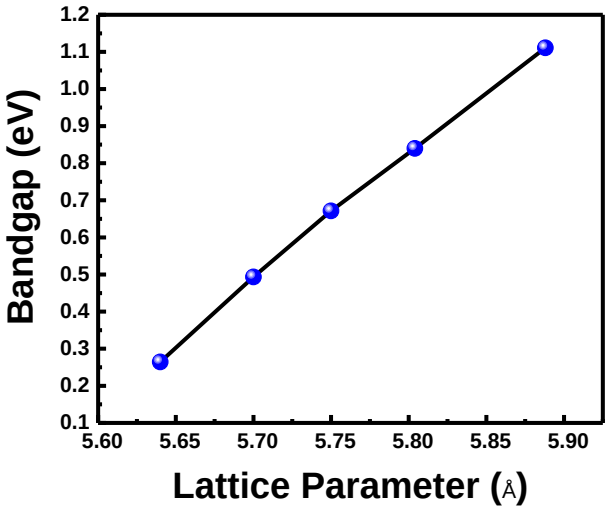

Figure S21. Calculated bandgap as a function of lattice parameter. The bandgap of $CsSnBr_3$ decreases substantially with a decrease of lattice parameter.

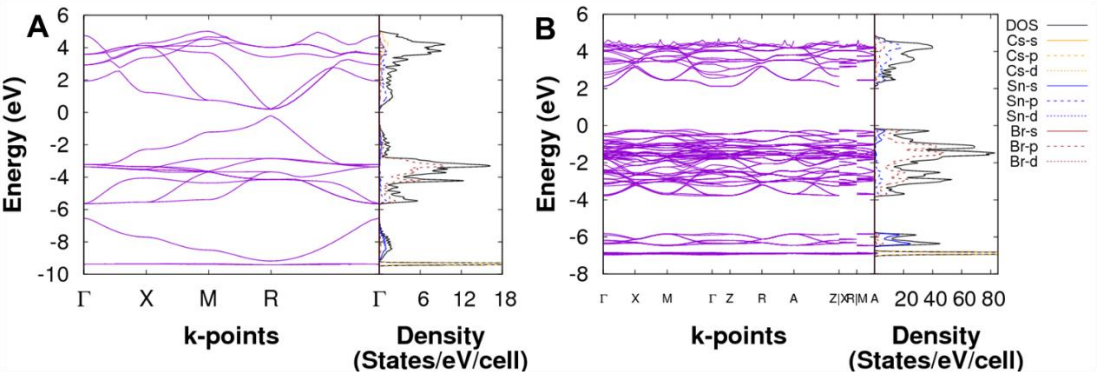

Figure S22. DFT calculation using the PBE functional. Band structure, density of states (DOS) and projected density of states (PDOS) of (A) $CsSnBr_3$ and (B) $CsSn_2Br_5$.

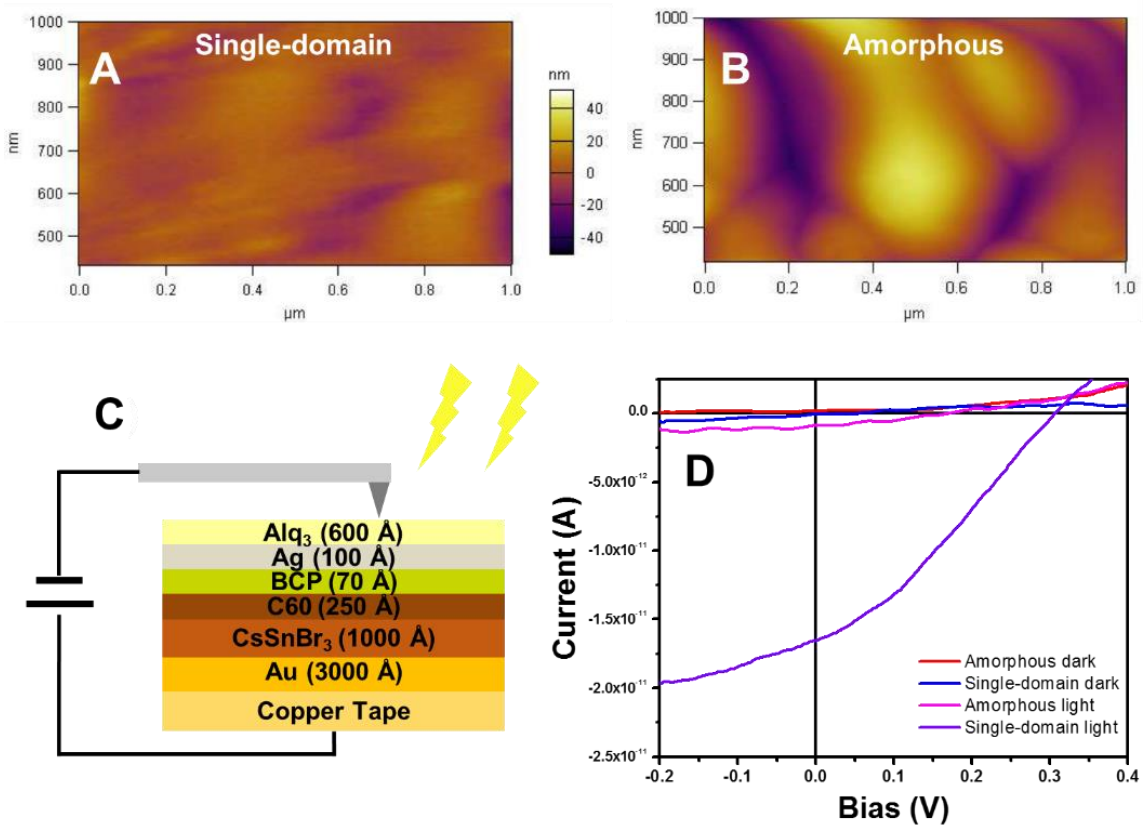

Figure S23. Solar cell device from epitaxial lift-off. AFM image of (A) single-domain epitaxial lift-off film, and (B) amorphous film. (C) Device architecture of the photovoltaic cells. (D) *I-V* curve of devices fabricated with the single domain epitaxy film and amorphous film, respectively, showing nearly an order of magnitude more photocurrent and double the voltage for single domain films versus the amorphous film.

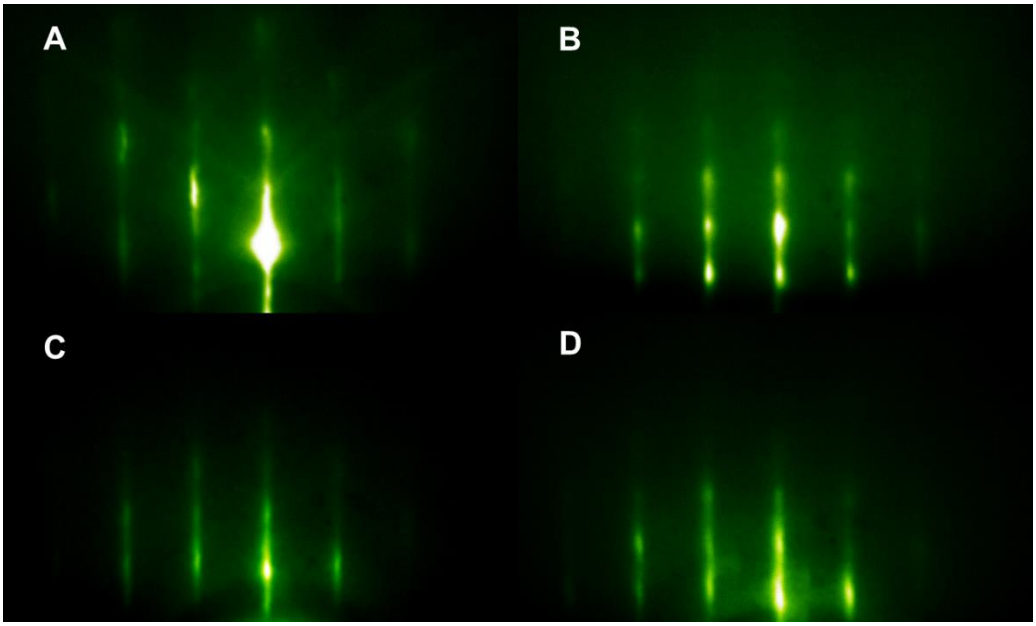

Figure S24. Multilayer quantum well fabrication. RHEED patterns of (a) freshly cleaved NaCl along [110] direction, (b) NaCl/$CsSnBr_3$(~10 nm)/NaCl(1.5 nm), (c) NaCl/$CsSnBr_3$(~10 nm)/NaCl(1.5 nm) /$CsSnBr_3$(~10 nm)/NaCl(1.5 nm),(d) NaCl/$CsSnBr_3$(~10 nm)/NaCl(1.5 nm) /$CsSnBr_3$(~10 nm)/NaCl(1.5 nm) /$CsSnBr_3$(~10 nm)/NaCl(1.5 nm). It indicates that with well controlled growth, no obvious change occurs even after growing three pairs of $CsSnBr_3$(~10 nm)/NaCl(1.5 nm). This provides opportunity for fabrication multi-junction quantum wells.

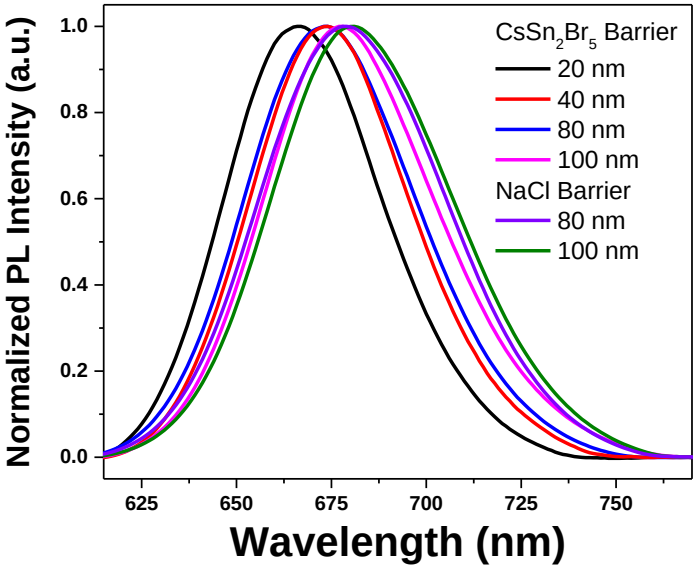

Figure S25. PL spectra of quantum well samples $CsSnBr_3$/$CsSn_2Br_5$ with various well widths: 20 nm (black curve), 40 nm (red curve), 80 nm (blue curve), 100 nm (magenta curve). PL of quantum well samples $CsSnBr_3$/NaCl as a comparison: 80 nm with NaCl (violet curve), and 100 nm with NaCl (olive curve).

Table S1. Lattice constants, film orientation and misfit of two phases.

Bulk Crystal Structure		$CsSnBr_3$	$CsSn_2Br_5$
		Pm3m, a=b=c=5.80 Å	I4/mcm, a=b=8.48 Å, c=15.28 Å
Precursor Ratio of CsBr to $SnBr_2$	0.25:1	-	Observed
	0.5:1	Observed < 2 ML	Observed > 3 ML
	1:1	Observed	-
	1.5:1	-	-
Orientation	Along NaCl [110]	[110]	[210]
	Along NaCl [100]	[100]	$[3\bar{1}0]$
	Along NaCl [001]	[001]	[002]
Misfit		-2.8 %	4.9 %

Table S2. Elemental ratio of as-deposited films obtained from XPS data.

Precursor Ratio	Real Ratio		
	Cs	Sn	Br
0.25:1	1.0±0.1	10.0±1.0	13.3±1.3
0.5:1	1.0±0.1	3.0±0.3	5.0±0.5
1:1	1.0±0.1	1.3±0.1	2.9±0.3

Table S3. Elemental ratio of as-deposited films obtained from XPS data collected after 1.5 min Ar^+ ion sputtering.

Precursor Ratio	Real Ratio		
	Cs	Sn	Br
0.25:1	1.0±0.1	4.0±0.4	5.5±0.6

Table S4. Calculated band gaps of $CsSnBr_3$ and $CsSn_2Br_5$ using the DFT-PBE and DFT-HSE06 methods.

Materials	PBE band gaps (eV)	HSE06 band gaps (eV)	Experimental value (eV)
$CsSnBr_3$	0.40	0.84	1.83±0.02
$CsSn_2Br_5$	2.33	3.12	3.34±0.04

Table S5. Emission energy of quantum well $CsSnBr_3$/NaCl with various well width.

Quantum Well Width (nm)	Emission Peak (nm)	Emission Energy (eV)
5	654	1.896
10	664	1.867
20	669	1.854
40	673	1.842
80	684	1.813
100	685	1.810

Table S6. Emission energy of quantum well $CsSnBr_3$/$CsSn_2Br_5$ with various well width.

Quantum Well Width (nm)	Emission Peak (nm)	Emission Energy (eV)
20	665	1.865
40	672	1.845
80	673	1.842
100	677	1.832
100 (NaCl)	681	1.821

Movie S1. *In-situ* real-time monitoring of the phase transition from cubic to tetragonal phase.

The phase transition from cubic to tetragonal phase arises after deposition is proceeding for around 20 s, which is interpreted as the film thickness of around 1-2 monolayers.

Supplementary Text

Computational Details

All the DFT calculations are performed using the Vienna Ab initio Simulation package (VASP) with the implemented projector augmented wave (PAW) potentials. All electronic self-consistent energy calculations converge within the accuracy of 10^{-5} eV between each electronic iteration. Gaussian smearing with the smearing width of 0.05 eV is used to treat bands with partial occupancies. For the cubic unit cell, an energy cutoff of the plane wave basis set (E_{CUT}) equal to 300eV and a Γ-centered 8×8×8 k-point mesh are used for both PBE and HSE06 calculation. For the tetragonal unit cell, using a gamma-centered 4×4×2 k-point mesh (i.e. k-point spacing of 0.03 $Å^{-1}$) was found to be suitable. For HSE06 calculations, we use E_{CUT} = 250eV, which yields an error of about 10 meV but reduces the computational cost. For PBE and HSE06 band structure calculations, paths connecting high-symmetry k-points are divided into 10-15 k-points. The high symmetry points in the plots are defined in Ref.[2]. For PBE DOS calculations, a finer grid of k-point that has the separation between k-points of around 0.01 $Å^{-1}$ is used, i.e. Γ-centered 16×16×16 and 11×11×6 grids are used for the $CsSn_2Br_5$ and $CsSnBr_3$ DOS calculations, respectively. For HSE06 DOS calculations, we use the gamma-centered 8×8×8 and 4×4×2 k-point meshes for $CsSnBr_3$ and $CsSn_2Br_5$, respectively. These grids result in a k-point spacing of around 0.02 – 0.03 $Å^{-1}$, which is sufficient for DOS calculations.

Fitting the Quantum Well data

The emission energy of a quantum well is described by the Brus equation as:[3]

$$E_g^{well}(L_z) = E_g^0 + \Delta E(L_z) = E_g^0 + \frac{\hbar^2\pi^2}{2m^*L_z} - \frac{1.8q^2}{4\pi\varepsilon_r\varepsilon_o L_z} \qquad (1)$$

where $E_g{}^0$ is the bulk band gap, ΔE is the confinement energy of both electrons and holes, $\hbar$ is reduced Planck constant, L_z is the thickness of the quantum well, and m^* is the reduced mass that can be obtained from the effective masses of the electron ($m_e{}^*$) and the hole ($m_h{}^*$) as $\frac{1}{m^*} = \frac{1}{m_e^*} + \frac{1}{m_h^*}$, q is the charge of electron, ε_r is the relative permittiviy, and ε_0 is the vacuum permittivity. Since the exciton binding energy of $CsSnBr_3$ has been reported to be less than 1 meV[4] the size dependence of the quantum well bandgap can be expressed as:[5]

$$E_{total} = E_g^0 + \Delta E = E_g^0 + \frac{\hbar^2\pi^2}{2m^*L_z^2} \qquad (2)$$

The value of m^* obtained by fitting the PL data of quantum well PL data can be extracted and then used for calculation of Bohr radius of this material by using Equation (3):[6]

$$a_B = \frac{4\pi\hbar^2\varepsilon\varepsilon_o}{e^2}\left(\frac{1}{m_e^*} + \frac{1}{m_h^*}\right) \qquad (3)$$

where a_B is the Bohr radius, e is the electron charge, ε_o is the vacuum permittivity, and ε is the dielectric constant of the semiconductor which has been reported for $CsSnBr_3$ to be 32.4.[4]

References:

[1] I. Abrahams, D. Z. Demetriou, R. T. Kroemer, H. Taylor, M. Motevalli, *Journal of Solid State Chemistry* 2001, **160**, 382.
[2] W. Setyawan, S. Curtarolo, *Computational Materials Science* 2010, **49**, 299.
[3] L. E. Brus, The Journal of Chemical Physics 1983, 79, 5566; L. Brus, *The Journal of Physical Chemistry* 1986, **90**, 2555.
[4] L.-Y. Huang, W. R. Lambrecht, *Physical Review B* 2013, **88**, 165203.
[5] D. A. Miller, *Quantum Dynamics of Simple Systems*, ed. G.-L. Oppo, SM Barnett, E. Riis, and M. Wilkinson (Institute of Physics, London, 1996) 1996, **239**.
[6] R. Koole, E. Groeneveld, D. Vanmaekelbergh, A. Meijerink, C. de Mello Donegá, in *Nanoparticles: Workhorses of Nanoscience*, (Ed: C. de Mello Donegá), Springer Berlin Heidelberg, Berlin, Heidelberg 2014, **13**.